Modeling divertor concepts for spherical tokamaks NSTX-U and ST-FNSF

IOP Publishing | International Atomic Energy Agency Nuclear Fusion
Nucl. Fusion 55 (2015) 086002 (8pp) doi:10.1088/0029-5515/55/8/086002

Special Topic

Modeling divertor concepts for spherical tokamaks NSTX-U and ST-FNSF

E.T. Meier[1,2], S. Gerhardt[3], J.E. Menard[3], T.D. Rognlien[1] and V.A. Soukhanovskii[1]

[1] Lawrence Livermore National Laboratory, Livermore, CA 94551, USA
[2] Present address: College of William and Mary, Williamsburg, Virginia 23187, USA
[3] Princeton Plasma Physics Laboratory, PO Box 451, Princeton, NJ 08543, USA

E-mail: emeier@wm.edu

Received 4 January 2015, revised 3 April 2015
Accepted for publication 24 April 2015
Published 22 July 2015

Abstract

The compact nature of the spherical tokamak (ST) presents an economically attractive path to fusion commercialization, but concentrates power exhaust, threatening the integrity of plasma-facing components. To address this challenge, experimentally constrained divertor modeling in the National Spherical Torus Experiment (NSTX) is extrapolated to investigate divertor concepts for future ST devices. Analysis of NSTX Upgrade with UEDGE shows that the secondary snowflake X-point position can be adjusted for favorable neutral transport, enabling stable partial detachment at reduced core densities. For a notional ST-based Fusion Nuclear Science Facility, divertor concepts are identified that provide heat flux mitigation ($<10\,\mathrm{MW\,m^{-2}}$) and low temperatures ($<10\,\mathrm{eV}$) compatible with high-Z targets. This research provides guidance for upcoming experiments and a basis for continued development of predictive capability for divertor performance in STs.

Keywords: spherical tokamak, divertor, UEDGE, snowflake

(Some figures may appear in colour only in the online journal)

1. Introduction

As fusion research progresses toward the reactor scale, increasingly intense power exhaust threatens the integrity of plasma facing components. The compact nature, i.e. small major radius (R), of the spherical tokamak (ST) presents an economically attractive path to fusion commercialization [1], but magnifies the power exhaust challenge, because the plasma-wetted area is proportional to R. To address this challenge, heat flux mitigation techniques, focusing on the snowflake divertor (SFD) configuration [2] and the effects of target tilt, have been considered for two future STs: the National Spherical Torus eXperiment Upgrade (NSTX-U) [3], and a notional ST-based Fusion Nuclear Science Facility (ST-FNSF) [1]. The relatively new SFD technique has been pursued experimentally on the TCV, NSTX, and DIII-D tokamaks [4–9].

Many heat flux mitigation techniques aim to induce detachment of the scrape-off layer (SOL) plasma from the divertor target(s). In detached operation, it is important to stabilize the cold, dense plasma in the divertor, preventing direct interaction with (and excessive cooling of) the core plasma. One way to achieve stable detachment is to detach a limited portion of the near SOL (e.g. within one heat flux width[4]), while the far SOL (beyond one heat flux width) remains attached—this corresponds to the planned partial detachment in ITER [11]. The transition to (partial) detachment can be characterized as a function of upstream density. A relatively low detachment density threshold may help to avoid density-related global stability limits and enable exploration of improved energy confinement expected in STs at low collisionality [3]. In the analysis presented below, detachment stability and threshold density will be highlighted.

A multi-fluid edge transport code, UEDGE [12, 13], has recently been used to analyze the SFD heat flux mitigation technique studied on NSTX [7]. Simulations captured the partial detachment observed experimentally in the SFD, reproducing the several-fold reduction of divertor heat flux, and 10-fold increase in divertor D_α brightness, while matching upstream plasma profiles [14]. The UEDGE analysis indicated that a combination of factors enabled stable, repeatable detachment in the SFD: (1) enhanced radiation (due to the large divertor volume); (2) power transmission to the targets through

[4] In the general sense implied here, the heat flux width is the exponential decay length (in the direction perpendicular to flux surfaces) of the heat flux deposited on the outer divertor and mapped to the outer midplane position; for detailed studies of the parametric dependence of heat flux width, more sophisticated definitions have been developed [10].

the neutral gas channel, which reduced electron temperature (T_e) below 0.5 eV, inducing volumetric recombination; and (3) increased recycling due to saturation of the lithium pumping mechanism. By demonstrating the ability of UEDGE to model ST detachment physics, the analysis provides a basis for the divertor concept research presented in this paper.

NSTX Upgrade (NSTX-U) will have up to 12 MW neutral beam power and 2 MA plasma current [3]. The expected unmitigated divertor target heat fluxes will be more than twice as high as observed in NSTX [15]. Initial NSTX-U SFD and conventional divertor (CD) configurations presented in [3] have been evaluated with UEDGE [16]. Limited advantage was seen for the SFD compared to the CD. While higher flux expansion at the outer target in the SFD case resulted in beneficial heat flux reduction near the outer strike point (OSP), this benefit was offset by detrimentally high inner target heat flux (>10 MW m^{-2}) and OSP temperatures exceeding 100 eV, presenting a sputtering concern. These problematic aspects of modeled SFD behavior were speculatively attributed to degraded neutral confinement, due to unfavorable orientation of the magnetic flux surfaces with respect to the target in the specific SFD configuration studied.

Section 2 presents an optimization of the SFD for NSTX-U, building on earlier modeling [14, 16]. In particular, the effect of snowflake X-point position on neutral confinement, and thus on detachment properties, is explored. Section 3 describes an assessment of divertor concepts for an ST-based Fusion Nuclear Science Facility (ST-FNSF) [1]. Conclusions are drawn in section 4.

2. NSTX-U modeling

2.1. Setup

Computational grids for UEDGE simulations of NSTX-U are based on five lower-single-null equilibria generated with ISOLVER, a free-boundary Grad–Shafranov equilibrium code [17]. The toroidal magnetic field is $B_t = 1$ T at the magnetic axis and the plasma current is $I_p = 2$ MA. The grids span from normalized flux $\psi_N = 0.9$ at the 'core-edge interface' (CEI) to a maximum extent of $\psi_N = 1.05$ in the SOL. Divertor regions of the five grids are shown in figure 1. The four SFD cases are each snowflake 'minus' configurations, i.e. the secondary X-point is in the SOL rather than the private flux region (PFR). At $I_p = 2$ MA, the projected heat flux width is 3 mm [15]. Dashed lines in figure 1 indicate flux tubes that, in the outer midplane (OMP), extend 3 mm from the separatrix into the SOL. The flux tubes clearly have expanded target footprints in the SFD cases. The divertor volume ($V_{\rm div}$), however, varies little between the five configurations: SFD-A and -B have the largest and smallest volumes, $V_{\rm div} = 0.19$ m^3 and $V_{\rm div} = 0.15$ m^3, respectively. Earlier research [16] studied only the CD and SFD-A. The present work evaluates an additional range of topologies given by SFD-B, -C, and -D, in which the secondary X-point is translated radially outward. (Note that present topological limitations of UEDGE prevent modeling SFD with secondary X-points inside the simulation domain; thus, such configurations are not considered here.)

Magnetic geometries of the SFD configurations are obviously modified with respect to the CD, as seen in figure 2, but subtle and, as will be shown, important differences exist

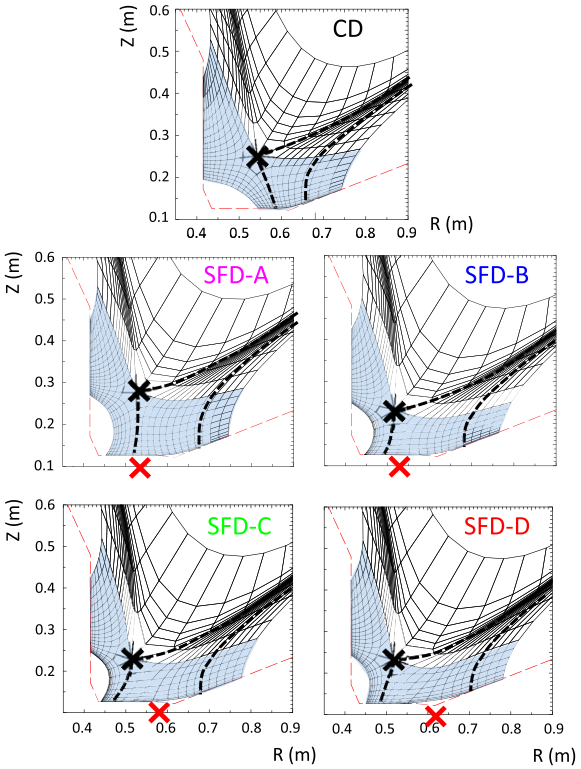

Figure 1. Divertor region of UEDGE grids for conventional divertor (CD) and snowflake divertor (SFD) simulations of NSTX-U. Primary and secondary (snowflake) X-points are shown with black and red Xs, respectively. Dashed lines indicate 3 mm flux tubes (corresponding to one heat flux width in the NSTX-U cases considered). Divertor volumes are indicated with blue shading.

between the four SFD. Geometric flux expansion is defined as $f_{\rm geo} \equiv f_{\rm exp}/\cos(\theta)$, where $f_{\rm exp}$ is the poloidal flux expansion, and θ is the 'target tilt'—the angular deviation from normal incidence of flux surfaces on the target. For SFD-A and -B, $f_{\rm geo}$ peaks near the separatrix, while for SFD-C and -D, the peaks are shifted radially outward. Connection lengths ($L_{\rm con}$) for the SFD cases are typically 50% greater than for the CD. The plot of θ shows that SFD-C and -D have $\theta > 0$ in most or all of the region corresponding to the 3 mm flux tube. Here, $\theta > 0$ indicates an acute angle between the outboard target and the flux surface. As discussed in detail below, for $\theta > 0$, neutral particles are guided toward the separatrix; for $\theta < 0$, the opposite is true. Notably, the flux surface tilting in SFD-C and -D resembles the magnetic geometry seen in the NSTX SFD experiments [7], and studied in associated modeling [14] as discussed in section 1.

The UEDGE settings presented here are intended to provide a qualitative representation of the NSTX-U edge plasma, and thus enable comparitive analysis of the divertor configurations considered. Density at the CEI ($n_{\rm core}$) is fixed for a given simulation, and varied in simulation scans as described below. Power through the CEI, split evenly between ion and electron channels, is 9 MW, corresponding to a high-power NSTX-U scenario with 12 MW neutral beam power, allowing for 25% power loss due to core radiation and fast ions. At the high-field-side (i.e. the inner wall), neutral

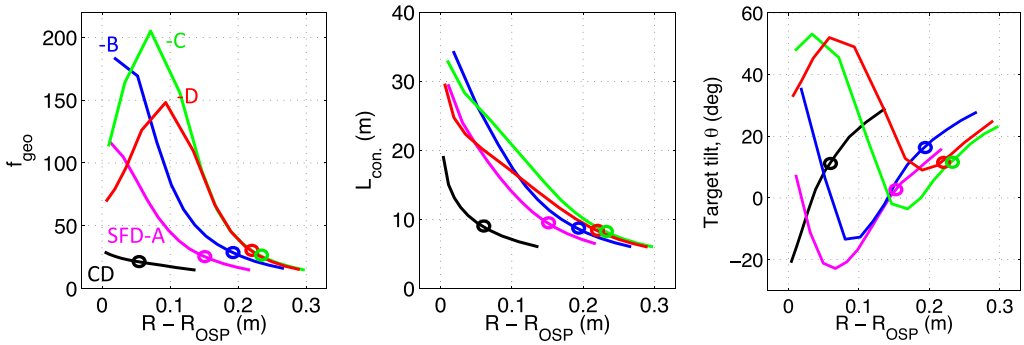

Figure 2. Magnetic geometries for UEDGE NSTX-U simulations. Geometric flux expansion (f_{geo}), midplane-to-target field line connection length (L_{con}), and 'target tilt' are shown as functions of radial position on the outer target with respect to the outer strike point (OSP) for the five configurations considered. Circular markers are placed at radial locations corresponding to 3 mm in the OMP.

gas is injected at a rate of $2.5 \times 10^{21}\,s^{-1}$. Perpendicular particle diffusivity (D) varies from $0.1\,m^2\,s^{-1}$ at the CEI to $0.5\,m^2\,s^{-1}$ at the separatrix and in the SOL, similar to D seen in transport analysis of H-mode NSTX discharges (e.g. [14, 18]). Perpendicular thermal diffusivities for ions and electrons ($\chi_{i,e}$) are $2\,m^2\,s^{-1}$ at the CEI, increase (as a cubic function of radius) to $4\,m^2\,s^{-1}$ at the separatrix, and are uniform in the SOL. The $\chi_{i,e}$ values of $2\,m^2\,s^{-1}$ at the CEI are typical of NSTX H-mode transport barriers [14, 18]. In the SOL, values of $4\,m^2\,s^{-1}$ were determined using the same approach as [16], i.e. targeting a 3 mm heat flux width in the CD case. All perpendicular diffusivities are poloidally uniform. At the outer wall, recycling is 90% for ions and neutrals, identical to the values used for NSTX simulations in which key divertor diagnostic measurements were matched [14]. Simulation results are not highly sensitive to the recycling choices at the outer wall. In the PFR, recycling, 90% for ions and 100% for neutrals, is again the same as used in NSTX modeling. The logic for the high neutral recycling in the PFR is that this small region is easily saturated; because detachment behavior is sensitive to PFR neutral pumping, since neutral densities rise as conditions approach detachment, it is important to model this saturation. At the targets, 99% ion recyling gives a modest particle removal rate consistent with boron-conditioned targets. Target recycling is 100% for neutrals, implying an (arbitrary) choice to allow target particle removal through only the ion channel. Charge-state-resolved carbon impurity modeling has proven difficult to validate in NSTX modeling [14]; therefore a simpler fixed concentration model is used here, with 3% carbon concentration—that is, everywhere in the domain, the total carbon density, used to compute carbon radiation, is 3% of the local electron density. At the outer and PFR boundaries, ion density and temperatures are assigned 2 cm gradient scale lengths. A model for neutral gas power transfer to divertor targets—which, as discussed in [14], is crucial to accurately modeling detachment with the UEDGE—is employed. Plasma drifts are not included.

2.2. Results and discussion

Significant variation is found in the detachment behavior of the five divertor configurations. Shown in figure 3 are results from a scan of CEI density (n_{core}) from 2×10^{19} to $4.5 \times 10^{19}\,m^{-3}$, with steps of $0.1 \times 10^{19}\,m^{-3}$. Total divertor ion inventories (N_{div}) for the CD, SFD-A, and -B are similar across the density range, rising slowly then abruptly increasing five-fold at $n_{core} \approx 4.5 \times 10^{19}\,m^{-3}$, corresponding to unstable detachment as discussed, e.g. in [19]; experimentally, such sudden detachment onset has recently been observed on the DIII-D tokamak [20]. In contrast, N_{div} values for SFD-C and -D are significantly higher, and rise more steadily. The Greenwald fraction (f_{GW}) (calculated as $f_{GW} \equiv \bar{n}/n_{GW}$, where $\bar{n}$ is estimated as three times the OMP separatrix density, consistent with NSTX data) is similar for all cases, and detachment occurs at values of f_{GW} appropriate for the NSTX-U mission [3]. For SFD-C and -D, $P_{rad,div}$ rises at lower n_{core} than the other cases, and exhibits a gradual rise similar to that seen for N_{div}. Total (non-radiative) power reaching the inner and outer divertor targets (Q_{div}) has a strong inverse correlation with N_{div} and $P_{rad,div}$. Particle input (Γ_{core}) from the injection of 12 MW neutral beam power is only $1.2 \times 10^{21}\,s^{-1}$, and would support only the lowest n_{core} values simulated. This implies that particle injection may be needed in NSTX-U high-power scenarios to achieve detached states, even when an optimal SFD configuration is implemented.

Regarding overall power flow, for low values of n_{core}, i.e. prior to detachment, the outer divertor in each case receives between 60 and 65% of the total divertor power. (After detachment, the inner/outer divertor power split varies more widely, but total deposited power is far reduced.) In each simulation, the power not deposited on divertor targets or radiated in the divertor—≈5 MW, or slightly more than 50%—is deposited on the outer wall.

At or below $4.7 \times 10^{19}\,m^{-3}$, all configurations exhibit detached conditions across most of the outer and inner targets, and the artificial grid boundaries strongly influence the solutions, apparently preventing complete collapse of the core plasma.

Detachment progresses radially across the outer target in the SFD-D scan of n_{core}, as illustrated in figure 4. At $n_{core} = 2 \times 10^{19}\,m^{-3}$, a small zone in the PFR has electron temperature (T_e) less than 2 eV (a typical indicator of detachment). SFD-D plots at $n_{core} = 2.8$ and $3.5 \times 10^{19}\,m^{-3}$ show that the detached zone spreads from the PFR to a location near $R - R_{OSP} = 0.20$ m on the outer target. Peak heat flux is $5.2\,MW\,m^{-2}$ at $n_{core} = 2.0 \times 10^{19}\,m^{-3}$, safely below $10\,MW\,m^{-2}$ (the typical technological limit); however, within the 3 mm flux tube (which extends to $R - R_{OSP} = 0.21$ m), T_e exceeds 50 eV. At

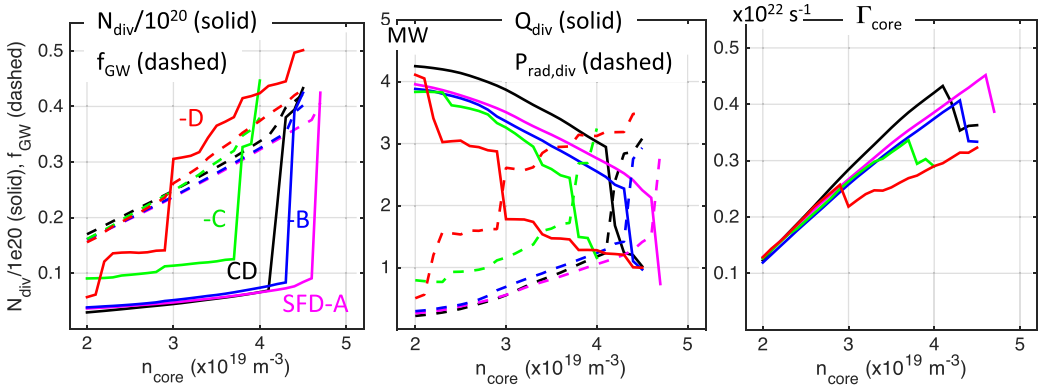

Figure 3. Results of density scan for NSTX-U configurations. Several key quantities are plotted as a function of core density: Greenwald fraction (f_{GW}) and the total divertor ion inventory (N_{div}) (left); total power (excluding radiation) reaching the divertor (Q_{div}) and power radiated in the divertor ($P_{rad,div}$) (center); particle flux through the core-edge interface (Γ_{core}) (right).

$n_{core} = 3.5 \times 10^{19}$ m^{-3}, peak heat flux is only slightly lower at 4.2 MW m^{-2}, but T_e is below 10 eV within the 3 mm flux tube; heat flux in that region is dominated by radiation, as shown. Because high target T_e can lead to excessive impurity sputtering and contamination of the upstream SOL, eliminating high target T_e in the near-separatrix region is mandatory to prevent subsequent core impurity buildup. Furthermore, SOL impurity transport analysis shows that high recycling conditions—low T_e and high density—tend to improve impurity retention in the divertor region [21]. The CD case has an unacceptable 16 MW m^{-2} peak outer target heat flux at $n_{core} = 2 \times 10^{19}$ m^{-3}. Target profiles for the CD case at $n_{core} = 2.8 \times 10^{19}$ m^{-3}, shown in figure 4, exhibit lower densities and higher temperatures (especially near the OSP) than in the corresponding SFD-D case, and heat flux is higher than even the low-density SFD-D case, largely due to the relatively small CD flux expansion.

Divertor target conditions in SFD-C are qualitatively similar to SFD-D. In SFD-A and -B, peak outer target heat flux is <6 MW m^{-2} across the range of n_{core} studied, but solutions show high temperatures inside the 3 mm flux tube except following sudden detachment at $n_{core} \approx 4.5 \times 10^{19}$ m^{-3}. Notably, all of the five divertor configurations have peak heat flux above 10 MW m^{-2} at the inner target at $n_{core} = 2 \times 10^{19}$ m^{-3}, but the inner target heat flux is mitigated to < 10 MW m^{-2} for $n_{core} > 2.3 \times 10^{19}$ m^{-3} for all configurations.

These UEDGE results suggest that seemingly subtle changes in secondary X-point location in the SFD can cause dramatic changes in detachment behavior. In SFD-D, for example, the detachment progresses continuously as core density is increased, whereas for SFD-A, detachment occurs abruptly at high core density. The existence of a gradual detachment transition offers operators some margin for error when aiming for partial detachment via, e.g. manual or automatic adjustment of divertor gas puffing or impurity injection; in divertors with abrupt detachment behavior, full detachment and X-point MARFE formation might be difficult to avoid when seeking partially detached states.

The gradual detachment in SFD-D is enabled by neutral transport physics. In UEDGE, the flux of neutral gas particles across flux surfaces (i.e. in the 'radial' direction) is given by $\Gamma_{g,r} = n_g v_{g,r}$. The radial neutral velocity is $v_{g,r} = \nabla_r p_g / (m_g n_g f_{xs})$, where m_g is the neutral particle mass, p_g is the neutral pressure, and f_{xs} is the sum of charge exchange and scattering collision frequencies. Ion recycling at targets naturally generates strong normal neutral pressure gradients. Assuming that ∇p_g is dominated by a component normal to the divertor target, $\nabla_r p_g = \nabla p_g \sin(\theta)$. Tangential components of ∇p_g may play a role, but results presented above suggest that 'tilt-induced' transport is dominant. SFD-C and -D, have θ up to 50° over the part of the target corresponding to the 3 mm flux tube (see figure 2), and the fact that detachment occurs in those cases at relatively low n_{core} is explained by the effect of target tilt on neutral transport. The gradual progression of detachment as a function of n_{core} in SFD-C and -D can also be understood in terms of tilt-induced transport. As detachment proceeds radially outward across the target, θ in SFD-C and -D is reduced from ~50° to $\lesssim$10°. The reduction of tilt-induced transport partially balances the increased density and radiation that typically occur as a detachment front moves upstream and, in this case, as the detached-to-attached transition point moves radially across the target as in figure 4. In [19], such a position-dependent reduction in transport and radiation is identified as a requirement for detachment stability.

The beneficial effects of flux surface tilting are well known. A vertical target configuration has been implemented and studied on, e.g. Alcator C-Mod [22], and is employed in the ITER divertor design [11]. The vertical target modifies θ by changes in the divertor hardware. In contrast, the SFD configuration allows similar modification of θ by changing the magnetic geometry. The modeling presented above suggests that such magnetic modification of θ can provide the advantageous effects of the vertical target configuration in an open divertor geometry like that of NSTX-U. Experimental research aimed at the physics observed in this modeling could be useful.

3. ST-FNSF modeling

3.1. Setup

Four ST-FNSF divertor configurations are modeled with UEDGE: a conventional divertor (CD); a CD with vertical target (CD-VT); a snowflake divertor (SFD); and a super-SFD,

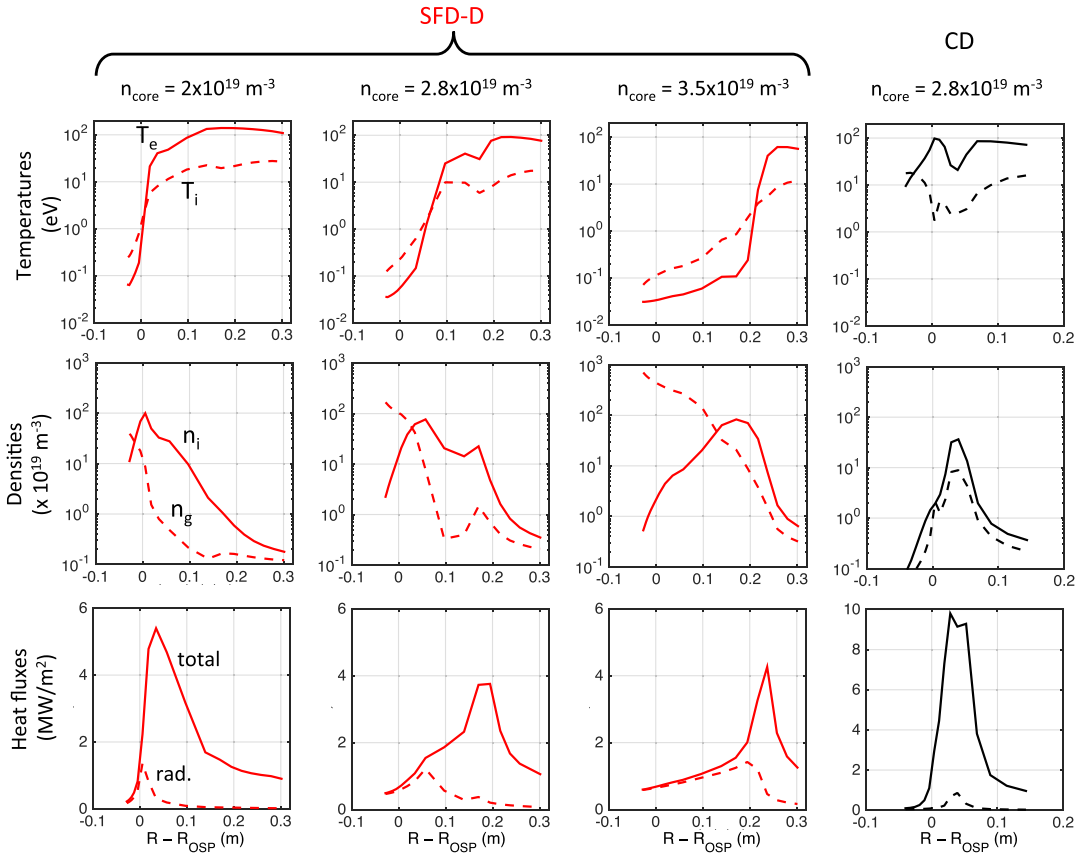

Figure 4. SFD-D and CD divertor target profiles. Temperatures (top row), densities (middle row) and heat fluxes (bottom row) are shown as a function of radial distance past the outer strike point ($R - R_{\mathrm{OSP}}$). For the SFD-D case, profiles are shown for three different densities; CD profiles are shown for a medium density case.

i.e, a SFD with extended outer divertor leg as in the Super-X divertor [23, 24]. Shown in figure 5 are computational grids for the four cases, based on up-down symmetric (i.e. balanced double-null) equilibria generated with ISOLVER. $B_t = 2.4\,\mathrm{T}$ at the magnetic axis and $I_p = 12\,\mathrm{MA}$. As for the NSTX-U simulations, the grids span ψ_N from 0.9 to 1.05.

Examining the magnetic geometries, the CD and CD-VT have similar geometric expansion, $f_{\mathrm{geo}} \approx 30$ near the OSP. The SFD has significantly more expansion, with $f_{\mathrm{geo}} \approx 55$ near the OSP, while the super-SFD has $f_{\mathrm{geo}} \approx 8$ near the OSP. Connection lengths are $L_{\mathrm{con}} \approx 20\,\mathrm{m}$ near the OSP for both CD and CD-VT cases, and $L_{\mathrm{con}} \approx 25$ and $50\,\mathrm{m}$ for the SFD and super-SFD, respectively. The CD and SFD cases have negative 'target tilt,' $\theta \approx -40^\circ$ across the targets, directing neutrals away from the OSP (see discussion of target tilt in section 2). In contrast, $\theta \approx 40^\circ$ and 80° across the CD-VT and super-SFD targets, respectively.

Power injection through the CEI is 30 MW, split evenly between ion and electron channels. Density at the CEI (n_{core}) is varied as in the NSTX-U modeling. At the outer walls, ion and neutral recycling is significantly higher than in NSTX-U simulations—99% versus 90%—representing the expected wall saturation in the long-pulse device. At the targets, 100% recycling of ions and neutrals represents fully saturated targets which might be made from a high-Z metal such as tungsten. PFR ion recycling is 99%, as for the outer walls. For neutral PFR recycling, whereas 100% PFR neutral recycling was assumed in NSTX-U modeling, 99% recycling is used here, implying a modest pumping mechanism to provide particle control in the inner divertor region. (Exceptions are made to these general PFR neutral recycling settings in the CD-VT and super-SFD cases, as discussed below.) Primary particle control is achieved via cryopumping, which is modeled by allowing neutral transmission through the surfaces indicated in figure 5. In the CD-VT case, transmission is 5%. In the other cases, transmission is 50%. To model neutral baffling in the super-SFD extended leg, neutral recycling is set to 100% for the surfaces with $R > 2\,\mathrm{m}$. Perpendicular transport cofficients are like the NSTX-U coefficients, except that the thermal transport is scaled down by a factor of two—this corresponds to the reduction in SOL heat flux width predicted by the heuristic drift-based model [25]. Nitrogen is included as a seeded impurity at 4% fixed concentration (a global constant as in NSTX-U modeling), and no intrinsic (sputtered) impurity is included. Gas power loss to the targets is included as in the NSTX-U cases. Gradient scale length boundary conditions are used for temperatures and densities at outer and PFR boundaries, with scale lengths set to 5 cm. Plasma drifts are not included.

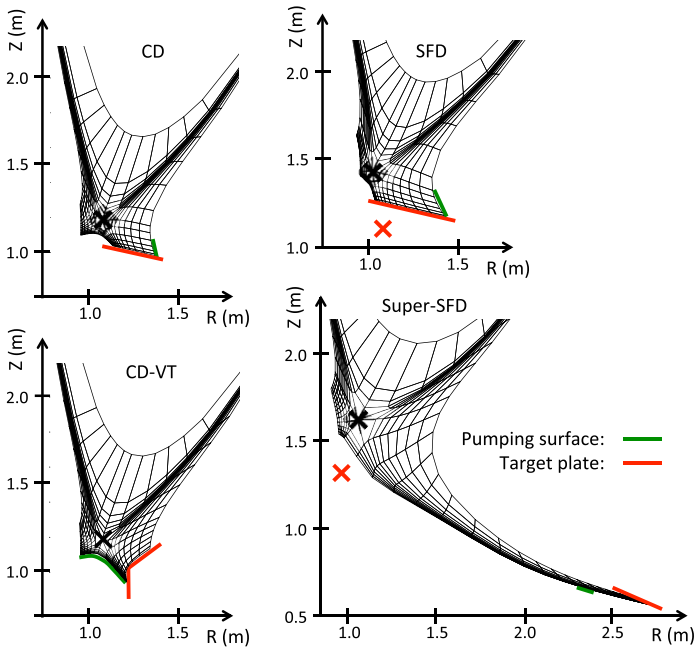

Figure 5. ST-FNSF grids. Primary and secondary (snowflake) X-points are shown with black and red X's, respectively. Divertor cryopump surfaces and targets are indicated.

3.2. Results and discussion

As illustrated by the results in figure 6, favorable particle trapping in the CD-VT and super-SFD cases results in much higher particle inventories and reduced divertor heat fluxes compared to CD and SFD cases at similar core density. This dichotomy is especially extreme in the super-SFD case, which has a geometry tailored for particle trapping. In the CD and SFD cases, target tilt—the same phenomenon identified in NSTX-U modeling as having a crucial role—is unfavorable, allowing rapid loss of neutral particles to the divertor cryopump surfaces. For each configuration, n_{core} is scanned from low to high, with steps of $0.2 \times 10^{19}\,\mathrm{m}^{-3}$. For the super-SFD case, at the lowest n_{core} value, divertor radiation and non-radiative heat deposition are similar; by $n_{\mathrm{core}} = 5 \times 10^{19}\,\mathrm{m}^{-3}$, complete transition to detachment has occurred, and radiated power is dominant. For the CD-VT case, the transition is in progress at the highest n_{core} values.

In divertor studies for ITER, Γ_{core} is used as a constraint for divertor optimization [26, 27]. Core particle input in ITER is limited to $\Gamma_{\mathrm{core}} \approx 5 \times 10^{22}\,\mathrm{s}^{-1}$ ($\approx$100 Pa m^3 s^{-1} $\approx$750 torr-liters s^{-1}). Here, a 'design point' of $\Gamma_{\mathrm{core}} = 1.9 \times 10^{22}\,\mathrm{s}^{-1}$ is selected for ST-FNSF (though this choice is inherently arbitrary because a complete ST-FNSF design has not been developed). Note that this implies significant auxiliary fueling beyond the neutral beam particle input of $\approx 4 \times 10^{21}\,\mathrm{s}^{-1}$. As seen in the plot of Γ_{core} in figure 6, at this design point, n_{core} varies significantly for the different configurations—$n_{\mathrm{core}} \approx$ 5.4, 6.0, 8.4, and $8.8 \times 10^{19}\,\mathrm{m}^{-3}$ for the CD, SFD, CD-VT, and super-SFD cases, respectively.

For all cases, inner target conditions are generally milder than outer target conditions, with lower T_e and heat flux; inner and outer SOL are disconnected, and three times more power is exhausted to the outer SOL than the inner SOL. In the CD and SFD design point cases, the outer divertor targets receive 70 to 80% of the total non-radiative divertor power. Outer targets in the CD-VT and super-SFD design point cases receive, respectively, 90% and 23% of the non-radiative divertor power. In the CD-VT, inner target detachment limits the power received there. In the super-SFD, the strongly detached plasma in the long leg results in power deposition that is significantly lower than the inner target (despite inner target detachment). In these ST-FNSF cases, the outer walls receive 20–30% of the input power. The reduction in wall power with respect to the NSTX-U cases (in which the outer walls received 50–60% of input power), is attributed to both a reduction of the cross-field transport coefficients, and the availability of four targets (instead of just two) to which power can be transmitted.

Figure 7 shows outer target profiles for the ST-FNSF cases at $\Gamma_{\mathrm{core}} = 1.9 \times 10^{22}\,\mathrm{s}^{-1}$ (the design point discussed above). In the CD and SFD cases, deposited heat fluxes are $<$10 MW m^{-2}, but unfavorable target tilt results in sheath-limited divertor plasmas, with target T_e within 10% of upstream T_e. In these cases, target T_e is in excess of 600 eV, which is unacceptable from a sputtering point of view, especially if the targets are composed of high-Z material. Notably, modified CD and SFD simulations with less target tilt (horizontal targets) yield conduction-limited target plasmas with heat fluxes exceeding 20 MW m^{-2}. With improved neutral confinement, CD-VT and super-SFD cases have $T_e < 10$ eV near the OSP, and outer target heat fluxes $<$10 MW m^{-2}. In the CD-VT, high outer target density is achieved through tilt-induced transport. For the super-SFD, however, tilt-induced transport is irrelevant—neutrals naturally accumulate in the closed end of the long leg, and the detachment front is localized near the cryopump duct. This behavior is analogous to water accumulating in a reservoir (the closed divertor leg) and eventually overflowing (into the

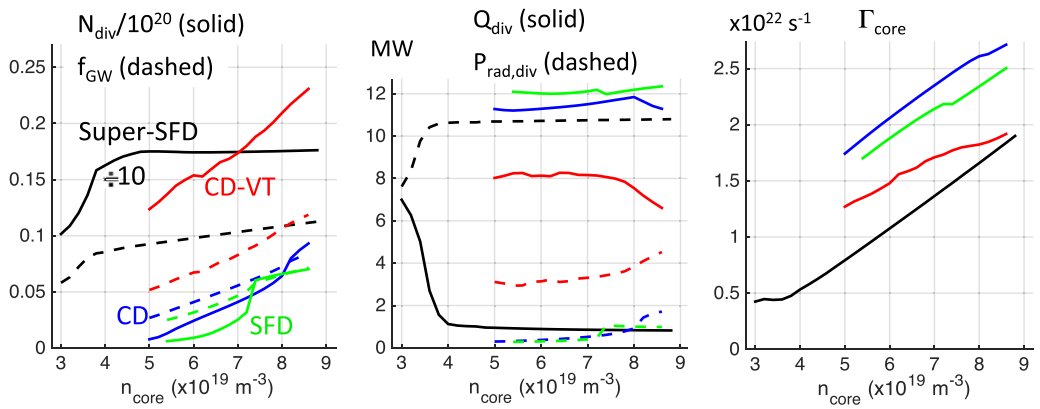

Figure 6. Results of density scan for ST-FNSF configurations. Several key quantities are plotted as a function of core density: Greenwald fraction (f_{GW}) and the total divertor ion inventory (N_{div}) (left); total power (excluding radiation) reaching the divertor (Q_{div}) and power radiated in the divertor ($P_{rad,div}$) (center); particle flux through the core-edge interface (Γ_{core}) (right). Note that N_{div} for the super-SFD configuration is divided by an additional factor of 10 such that $N_{div}/10^{21}$ is plotted. Integrated divertor quantities are for the lower (inner and outer) divertor only; up-down symmetry is assumed in the modeling.

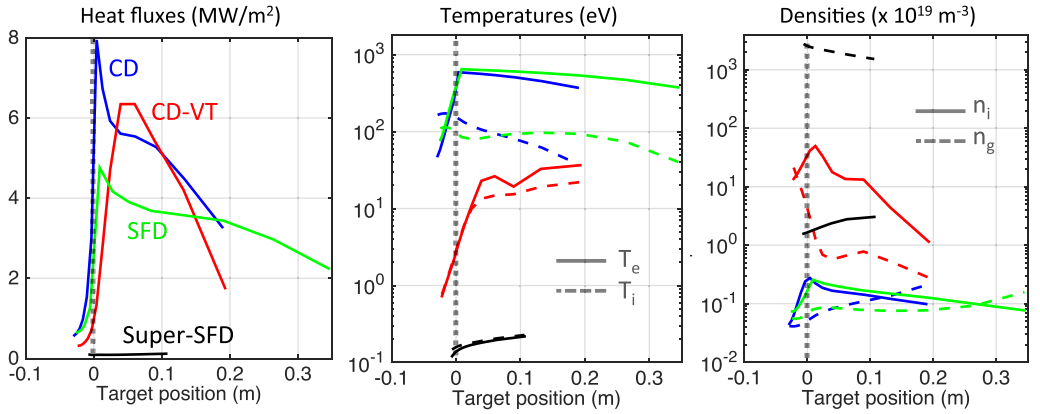

Figure 7. ST-FNSF outer target heat fluxes, temperatures, and densities, plotted versus. position along the outer target relative to the outer strike point. (Positive and negative positions refer to the SOL and private flux region, respectively.) These profiles are for the 'design point' cases at $\Gamma_{core} = 1.9 \times 10^{22}\,s^{-1}$, i.e. $n_{core} = 5.4$, 6.0, 8.4, and $8.8 \times 10^{19}\,m^{-3}$ for the CD, SFD, CD-VT, and super-SFD, respectively.

cryopump duct). Super-SFD simulations with no target tilt yield similar full detachment. Furthermore, simulations in which the cryopump duct is moved up and down the outer divertor leg show that the detachment front (defined as the location at which T_e is reduced to 2 eV) simply tracks the cryopump duct position.

The contrast between the divertor plasma properties in the four cases reflects enormous differences in global recycling behavior. In the CD and SFD, particles are directed radially outward toward the cryopump ducts, giving low densities and low global recycling. In the CD-VT, and especially in the super-SFD, favorable geometry traps divertor particles, resulting in high densities and high global recycling. For the design point cases, the total wall particle fluxes (Γ_{wall}) (including fluxes to divertors, outer walls and the PFR) are $\Gamma_{wall} = 5.4$, 5.8, 21.5, and $72.1 \times 10^{22}\,s^{-1}$ in the SFD, CD, super-SFD, and CD-VT cases, respectively. Calculating the global recycling as $R_{global} = 1 - \Gamma_{core}/\Gamma_{wall}$ gives $R_{global} = 65\%$ (SFD), 67% (CD), 91% (super-SFD), and 97% (CD-VT).

Of the 30 MW input power, only 2% is radiated by nitrogen in the CD and SFD cases. In the super-SFD and CD-VT cases, 37% and 25% of the input power is radiated by nitrogen. The reason for this disparity is that the radiative cooling rate (in $W \cdot m^3$) for nitrogen peaks near 12 eV, and drops dramatically for higher temperatures. The CD and SFD, as modeled, are too hot for nitrogen to act as a radiator. Impurities that radiate strongly at high temperatures (e.g. several hundred eV) can be detrimental to core confinement; thus, it is preferable to identify divertor configurations, like the super-SFD and CD-VT, that engage low-temperature radiators.

Note that the SFD here are 'quasi-snowflakes' in the sense that the inter-X-point distance exceeds the heat flux width mapped to the primary X-point position. The near-target expansion in the SFD case provides the expected geometric heat flux reduction. In the super-SFD, though, the secondary

X-point is far from the outer target, and probably has a minor effect on the UEDGE results.

4. Conclusions

Prior UEDGE modeling of the NSTX-U SFD [16] indicated that SFD divertor optimization should be considered to achieve favorable neutral confinement and thus avoid sheath-limited outer target plasma conditions. In pursuit of such optimization, several different SFD configurations are studied and compared. In SFD cases A, B, C, and D, the secondary X-point is translated horizontally across the outer target. Modeling of the four SFD cases and a conventional divertor case shows that SFD-C and -D configurations enable highly radiating, partially detached divertor conditions at relatively low core densities, and also provide a gradual detachment as core density is increased. This favorable result is attributed to improved neutral confinement as flux surfaces are tilted with respect to the target in SFD-C and -D. The impact of flux surface tilt in the SFD configuration has not been explicitly considered experimentally; such an investigation could be an interesting subject for future research.

Modeling of ST-FNSF divertor configurations indicates that control of neutral behavior is crucial to achieving low target temperature compatible with low sputtering yields. By managing neutral behavior with target tilt (CD-VT) or extension and baffling of the outer divertor leg (super-SFD), acceptable target temperatures ($<$50 eV) are achieved. In the CD-VT, neutrals are directed toward the outer strike point, promoting outer strike point detachment ($T_e \approx 2$ eV). In the super-SFD, full outer target detachment is seen, with the upstream cryopump duct providing natural detachment front stabilization. An experimental investigation of such cryopump-derived stabilization could be pursued in a machine like Alcator-DX [28], which, as presently conceived, has an appropriate long outer divertor leg and upstream cryopump position.

This research provides guidance for upcoming experiments and a basis for continued development of predictive capability for divertor performance in STs. Numerous avenues remain to be explored in future ST divertor and SOL modeling. The UEDGE neutral model is limited to flux-aligned grids similar to those presented here, but Monte Carlo neutral codes with greater flexibility are available, e.g. through the SOLPS package [29]. More flexible neutral modeling can more accurately represent geometric features such as neutral baffling and cryopump ducts. Charge-state-resolved impurity modeling should be developed and validated for the H-mode ST. As discussed in [14], the inclusion of drift physics might be necessary to capture, even qualitatively, impurity transport behavior. Finally, several snowflake effects, such as instability-driven mixing in the region of weak poloidal field [30], are not included in this UEDGE modeling, and might play an important role.

Acknowledgments

Discussions with LLNL scientists D.D. Ryutov, M.V. Umansky, M.E. Rensink, and G.D. Porter, about divertor and snowflake physics, and about UEDGE, have been much appreciated. Special thanks also to D.A. Gates and F.M. Poli of PPPL, who provided valuable advice for running ISOLVER. Insightful input from the referees is also gratefully acknowledged. This work was performed under the auspices of the U.S. Department of Energy by Lawrence Livermore National Laboratory under Contracts DE-AC52-07NA27344 and DE-AC02-09CH11466. This material is based upon work supported by the U.S. Department of Energy, Office of Science, Office of Fusion Energy Sciences.

References

[1] Menard J.E. *et al* 2011 *Nucl. Fusion* **51** 103014
[2] Ryutov D.D. 2007 *Phys. Plasmas* **14** 064502
[3] Menard J.E. *et al* 2012 *Nucl. Fusion* **52** 083015
[4] Piras F. *et al* 2009 *Plasma Phys. Control. Fusion* **51** 055009
[5] Vijvers W.A.J. *et al* 2014 *Nucl. Fusion* **54** 023009
[6] Soukhanovskii V.A. *et al* 2011 *Nucl. Fusion* **51** 012001
[7] Soukhanovskii V.A. *et al* 2012 *Phys. Plasmas* **19** 082504
[8] Hill D. *et al* 2013 *Nucl. Fusion* **53** 104001
[9] Soukhanovskii V.A. *et al* 2015 *J. Nucl. Mater.* in press (doi: 10.1016/j.jnucmat.2014.12.052)
[10] Eich T. *et al* 2011 *Phys. Rev. Lett.* **107** 215001
[11] Loarte A. *et al* 2007 *Nucl. Fusion* **47** S203
[12] Rognlien T.D. *et al* 1992 *J. Nucl. Mater.* **196** 347
[13] Rognlien T.D. and Rensink M.E. 2002 *Fusion Eng. Des.* **60** 497
[14] Meier E.T. *et al* 2015 *J. Nucl. Mater.* in press (doi: 10.1016/j.jnucmat.2015.01.007)
[15] Gray T.K. *et al* 2011 *J. Nucl. Mater.* **415** S360
[16] Meier E.T. *et al* 2014 *Contrib. Plasma Phys.* **54** 454
[17] Huang J. and Menard J. 2005 *Bull. Am. Phys. Soc.* **47** GP1.45
[18] Canik J.M. *et al* 2011 *J. Nucl. Mater.* **415** S409
[19] Hutchinson I.H. 1994 *Nucl. Fusion* **34** 1337
[20] McLean A.G. *et al* 2015 *J. Nucl. Mater.* in press (doi: 10.1016/j.jnucmat.2015.01.066)
[21] Scotti F. 2014 *PhD Thesis* Princeton University
[22] Lipschultz B. *et al* 2007 *Fusion Sci. Technol.* **51** 369
[23] Valanju P.M. *et al* 2009 *Phys. Plasmas* **16** 056110
[24] Havlickova E. *et al* 2014 *Plasma Phys. Control. Fusion* **56** 075008
[25] Goldston R.J. 2012 *Nucl. Fusion* **52** 013009
[26] Kukushkin A. *et al* 2001 *J. Nucl. Mater.* **290** 887
[27] Kukushkin A. S. *et al* 2011 *J. Nucl. Mater.* **415** S497
[28] LaBombard B. *et al* 2013 *Bull. Am. Phys. Soc.* **58** CO4.2
[29] Schneider R., Bonnin X., Borrass K., Coster D.P., Kastelewicz H., Reiter D., Rozhansky V.A. and Braams B.J. 2006 *Contrib. Plasma Phys.* **46** 3
[30] Ryutov D.D. *et al* 2012 *Plasma Phys. Control. Fusion* **54** 124050